Energy & Environmental Science

Tracking ion intercalation into layered Ti_3C_2 MXene films across length scales

Journal:	*Energy & Environmental Science*
Manuscript ID	EE-ART-05-2020-001580.R1
Article Type:	Paper
Date Submitted by the Author:	06-Jul-2020
Complete List of Authors:	Gao, Qiang; Oak Ridge National Laboratory Sun, Weiwei; Oak Ridge National Laboratory, Center for Nanophase Materials Sciences; Key Laboratory of MEMS Ministry of Education, bSEU-FEI Nano-Pico Center Ilani-Kashkouli, Poorandokht ; Georgia State University Tselev, Alexander; Universidade de Aveiro, CICECO Kent, Paul; Oak Ridge National Laboratory Kabengi, Nadine; Georgia State University, Geosciences Naguib, Michael; Tulane University, Physics and Engineering Physics; Tulane University Alhabeb, Mohamed; Drexel University tsai, wan yu; Oak Ridge National Laboratory Baddorf, Arthur; Oak Ridge National Laboratory Huang, Jingsong; Oak Ridge National Laboratory Jesse, S.; Oak Ridge National Laboratory Gogotsi, Yury; Drexel University Balke, Nina; Oak Ridge National Laboratory

ARTICLE

Received 00th January 20xx,

Accepted 00th January 20xx

DOI: 10.1039/x0xx00000x

Tracking ion intercalation into layered Ti_3C_2 MXene films across length scales

Qiang Gao[a‡], Weiwei Sun[a, b*‡], Poorandokht Ilani-Kashkouli[c], Alexander Tselev[d], Paul R. C. Kent[a,e], Nadine Kabengi[c], Michael Naguib[f], Mohamed Alhabeb[g], Wan-Yu Tsai[a], Arthur P. Baddorf[a], Jingsong Huang[a,e], Stephen Jesse[a], Yury Gogotsi[g], Nina Balke[a*]

Enhancing the energy stored and power delivered by layered materials relies strongly on improved understanding of the intricate interplay of electrolyte ions, solvents, and electrode interactions as well as the role of confinement. Here we report a highly integrated study with multiscale theory/modelling and experiments to track the intercalation of aqueous Li^+, Na^+, K^+, Cs^+, and Mg^{2+} ions into Ti_3C_2 MXene. The integrated analysis of experiments assisted by theory/modelling allows for a deep understanding of energy storage processes highlighting the importance of the dynamics of cations, their positionings between MXene sheets, their effects on mechanical properties and capacitive energy storage. Computational simulations and *operando* calorimetry measurements proves the processes involving cation dehydration and H^+ rehydration, showing good correlation for heat variations between experiments and theory. *Operando* liquid AFM mapped energy dissipation of ions appears non-uniformly across the MXene surface, indicating heterogeneities of ions inside the MXene and confirming partially the ion behaviour obtained in theory. We directly demonstrate that the average distance between the cation and MXene surface follows a modified two-sided Helmholtz model when plotted versus the open circuit potential capacitance, revealing a different electrical double layer mechanism in confinement. This new fundamental understanding lays the foundation for improved functional devices utilizing electrodes and membranes made of two-dimensional materials.

Broader context

Intercalation capacitance has emerged as an alternative chemistry for enhancing energy stored and power delivered by supercapacitors. Two-dimensional metal carbide/nitride termed MXenes discovered in 2011 present very promising intercalation volumetric capacitance with ultrafast ion transport. A fundamental understanding of energy storage chemistry under the confinement is critical for enhancing the amount of energy stored in MXenes, which however remains elusive. In this contribution, we develop multiscale and multidisciplinary experimental-theoretical approaches to elucidate the confined complexity of the intercalation interactions of cation, water, and MXene surface. The findings help to guide further development in the large MXenes family and will be rapidly adopted to enable manipulating behaviours of ions and confined fluids for a variety of capacitive energy technologies.

[a]Center for Nanophase Materials Sciences, Oak Ridge National Laboratory, Oak Ridge, TN 37831, USA

[b]SEU-FEI Nano-Pico Center, Key Laboratory of MEMS of Ministry of Education, Southeast University, Nanjing 210096, China

[c]Department of Geosciences, Georgia State University, Atlanta, GA 30303, USA

[d]Department of Physics and CICECO-Aveiro Institute of Materials, University of Aveiro, 3810–193 Aveiro, Portugal

[e]Computational Sciences and Engineering Division, Oak Ridge National Laboratory, Oak Ridge, TN 37831, USA

[f]Department of Physics & Engineering Physics, 2001 Percival Stern Hall, Tulane University, New Orleans, LA 70118

[g]Department of Materials Science and Engineering & A.J. Drexel Nanomaterials Institute, Drexel University, Philadelphia, PA 19104, USA

Corresponding author: Nina Balke, balken@ornl.gov (experiment), Weiwei Sun, sunw@ornl.gov (theory)

‡ equally contributing authors

Electronic Supplementary Information (ESI) available. See DOI: 10.1039/x0xx00000x

Intercalation of ions in active electrode materials is extremely critical for many electrochemical energy storage systems. Layered materials are especially attractive due to their ultra-fast intercalation kinetics[1-3]. MXenes[4, 5], a rapidly growing class of two-dimensional (2D) hydrophilic and layered metallic conductive materials, have shown promising intercalation capacitance and kinetics in neutral and acidic aqueous solutions[6, 7]. The most studied MXene to date, *i.e.*, Ti_3C_2, has achieved striking volumetric capacitance up to 1500 F cm^{-3} and areal capacitance up to 4 F cm^{-2} in aqueous H_2SO_4 electrolyte[8]. Ultra-high-rate capacitive performance up to 100 V s^{-1} has been realized through a 90-nm-thick Ti_3C_2[8] or vertically aligned MXene in aqueous 3M H_2SO_4[9], surpassing many other state-of-the-art capacitive materials[8]. The charging mechanism shows a strong dependence on the electrolyte used. The electrochemically reversible redox (pseudocapacitive) mechanism in acidic electrolyte and the electric double layer (EDL) response in neutral aqueous media have been demonstrated by *in situ* X-ray absorption[10] (XAS) and Raman spectroscopy[11], respectively. Wang *et al.* demonstrated the pseudocapacitive Li^+ intercalation using Ti_3C_2 MXene in lithium bis(trifluoromethanesulfonyl)imide (LiTFSI) with different organic solvents, and efficient desolvation of Li^+ from propylene carbonate

solvent results in high volumetric capacitance and fast charge transport[12]. However, non-flammable and non-corrosive, safe, environmentally benign, relatively high voltage, and low cost characteristics leave neutral aqueous electrolytes as a better alternative for industry[13, 14].

Increasing the amount of energy stored in MXenes requires improved understanding of the interfacial chemistry of cations including the interactions of cation, water, and MXene surface under confinement. Cations intercalated into MXene interlayers can remarkably affect the interlayer spacing, the dynamics of confined water, or electrical conductivity, etc[6, 15-17]. In addition, confined water noticeably improves the energy and power density of MXenes[18, 19]. X-ray diffraction (XRD)[20], electrochemical quartz crystal microbalance (EQCM)[18, 21-23] and neutron scattering techniques[16, 24] further provide insight into the extent of MXene volume variations and their correlations with the quantity of co-intercalated water. This is complemented by findings based on electrochemical dilatometry and atomic force microscopy (AFM) on changes in electrode volume and mechanical stiffness as a result of cation intercalation[25-27]. A more recent communication demonstrates cation intercalation dramatically alter the oxidation state of Ti atoms in Ti_3C_2 MXenes via XAS.[28] To develop a fundamental understanding of the ion intercalation processes, theory in combination with experiments is often used. For instance, ReaxFF GCMC was applied to study the diffusivity of the monolayer of water and the dynamics of cations[24]. Yamada *et al*. studied the capacitance by using of the solvation model[19]. Although both reported good agreement with experiments, the less verified theoretical parameters and the lack of explicit water are expected to lead to incorrect solvation environment and the cation-MXene interactions, which are of great importance to capacitive performances but less studied[19].

In this study, we demonstrate highly integrated approaches combining multiscale simulations/modelling and multidisciplinary experiments to elucidate: i) how aqueous cations interact with water molecules and Ti_3C_2 MXene surfaces under confinement; and ii) what the consequences are for other relevant processes including capacitive energy storage. We started by performing *ab initio* molecular dynamics (AIMD) calculations to reveal the preferred positions of the monovalent Li^+, K^+, Na^+, Cs^+, and divalent Mg^{2+} cation within the confinement of MXene and the surrounding hydration environment showing their significantly different behaviours. The use of AIMD was chosen due to its high accuracy needed for the characterization of ion-water interactions, facilitating understanding interactions in the confined MXenes layers non-empirically and correlating them to the energetic and capacitive properties. The local density functionals used have been shown to have a good match with structural and capacitive properties of MXene.[29-32] The overall energetics of the cation adsorption were measured directly via *operando* flow microcalorimetry (FMC) and consequences of cation adsorption, *i.e.*, H^+ release, were measured experimentally. Out of the complicated reactions, the theoretically modelled heat change from two processes (cation dehydration and H^+ rehydration) was in a qualitative agreement with calorimetry data. The influence of the cations on the water network on the atomic level within the confinement affects local energy dissipation, as measured on length scales of 10s' nanometers via *operando* AFM. Most interestingly, the simulated distance between cations and the MXene surface can be linked to the macroscopically measured capacitance at the open circuit potential (OCP). This shows a *1/d* relationship with an additional residual capacitance. We propose a modified two-sided EDL Helmholtz model to explain the observed capacitance trends and identify EDL formation as main energy storage process in neutral aqueous electrolytes. A good agreement between multiscale modelling and multidisciplinary experiments lays a strong foundation for enhancing energy storage properties of a variety of 2D and layered materials.

Results and discussion

To prepare the ground to rationalize the subsequent experimental studies, we first investigate the intercalation states of Li^+, Na^+, K^+, Cs^+ and Mg^{2+} cations inside the slit pores of MXene using AIMD simulations. Anions are not considered due to the fact that MXene surface are negatively charged,[7] leading to the expulsion of anions and intercalation of cations. This assumption might not be true for larger electrochemical voltage windows in a full battery or capacitor with MXene electrodes. In those cases, the intercalation of anions will need to be considered as well. In addition, during electrochemical cycling, only cation intercalation is probed due to the oxidation of MXene at positive potentials. Fig. 1a shows representative atomic arrangements around different cations confined in two MXene layers. These clearly demonstrate the effect of confinement on the cation. Each cation exhibits a different affinity towards water molecules and the MXene surface. Li^+, Na^+ and K^+ display specific adsorption on the pore surface while Cs^+ and Mg^{2+} are located in the pore center. It is worth noting that among all cations studied, the Na^+ ion caused a disordered structure of MXene. Ren *et al.* have reported the penetration of Na^+ into Ti_3C_2 MXene membrane, which exhibits the highest permeation rate amongst the studied cations and adsorption to MXene surface[33], supporting the AIMD findings.

We further quantify the relative positions between cation and the oxygen in water (-O_W) as well as the oxygen as part of the MXene surface termination (-O_T) by radial distribution functions (RDF), $g(r)$. As presented in Fig. 1b, Li^+ and Mg^{2+} exhibit the shortest cation-O_W distance, which can be interpreted as having the smallest hydration shell radii while Cs^+ has the largest hydration radius in confinement. The distance between the cation and oxygen is determined by the maximum of the $g(r)$ radial distribution function whereas error bars are extracted from the standard deviation of a gaussian curve fit to describe the first ion shell. More details are given in Fig. S1, ESI. As shown in Fig. 1c, the distance between cation and O_W scales linearly with the respective values in the bulk water[34] demonstrating that the 1st shell hydration radius is not affected by confinement. We note that the hydrated cation size intimately follows the results of a recent EQCM study on Ti_3C_2 MXene. As reported by Shpigel *et al*., the hydrophilic Li^+, Na^+, Mg^{2+}, and Al^{3+} cations co-inserted with larger amounts of water compared to the hydrophobic K^+, Cs^+, and TEA^+, which reduced the retained water in the interlayer confinement.[18] This effect is believed to be due to intercalations of cations and their interactions with water/MXene under confinement. When comparing the number of water molecules per cation m_w with the cation-O_W distance, it can be seen that extra water enters the Ti_3C_2 MXene when the cation-water

distance becomes smaller than the Ow-Ow distance and that water is expelled from the electrode when the cation-water distance becomes larger than the Ow-Ow distance (Fig. S2, ESI).

In contrast to the solvation shell radii, the coordination numbers (CN) of the confined cations are clearly reduced compared to bulk values (Fig. 1d), indicating all cations undergo a partial dehydration upon entering the confined spaces of MXene. For Li^+, Na^+, and K^+, the surface oxygen Ow and termination oxygen O_T are equidistant, and both contribute to the number of oxygens surrounding the cation. In the case of Cs^+ and Mg^{2+}, only Ow is taken into account due to their large distances from the MXene surface (Fig. S3, ESI). These results clearly demonstrate the effect of confinement on the cation hydration.

To further explore cation intercalation process, we employed *operando* FMC to unravel the energetics that governs the water-cation exchange as a function of time. Ti_3C_2 MXene was homogeneously packed into the FMC micro-column and equilibrated with deionized water before the input solution was changed to a solution containing one of the following salts Li_2SO_4, Na_2SO_4, K_2SO_4, Cs_2SO_4, or $MgSO_4$ at a concentration of 0.5 M. For all solutions, the initial pH was adjusted to 5.6 ± 0.2. A consequence of metal cation intercalation is the reduction of CN of ions (Fig. 1d) and, in case of absorption onto -OH terminated MXene surfaces, the release of H^+ according to the conceptual Eq. 1. To quantify this process, *in situ* pH measurements were performed during the calorimetry experiment.

$$Ti_3C_2-OH + M(H_2O)_x^+ \rightarrow Ti_3C_2-O-M(H_2O)_{x-y} + H^+ + yH_2O \quad (1)$$

The resulting calorimetric signal curves reflect the sum of transient energies for all involved processes most notably the dehydration of the intercalated cation which is an endothermic process, and the rehydration of the desorbed H^+ which is an exothermic process (Fig. 2a). For instance, the net exothermic calorimetric signal of Na^+ adsorption includes endothermic reaction, *i.e.*, the smaller bulk hydration enthalpy of Na^+ (ΔH_{hyd} = -409 kJ mol^{-1}), and the larger bulk hydration enthalpy of desorbed H^+ (-1091 kJ mol^{-1}) that is exothermic. The measured heat of reaction (HOR) does show a synchronous trend with the atomic size of the cations, where that of Li^+ intercalated MXene has the greatest modulation of heat because of long-lasting endothermic signal at the beginning of ~15 min visible in Fig. 2a. Details about the HOR will be discussed below.

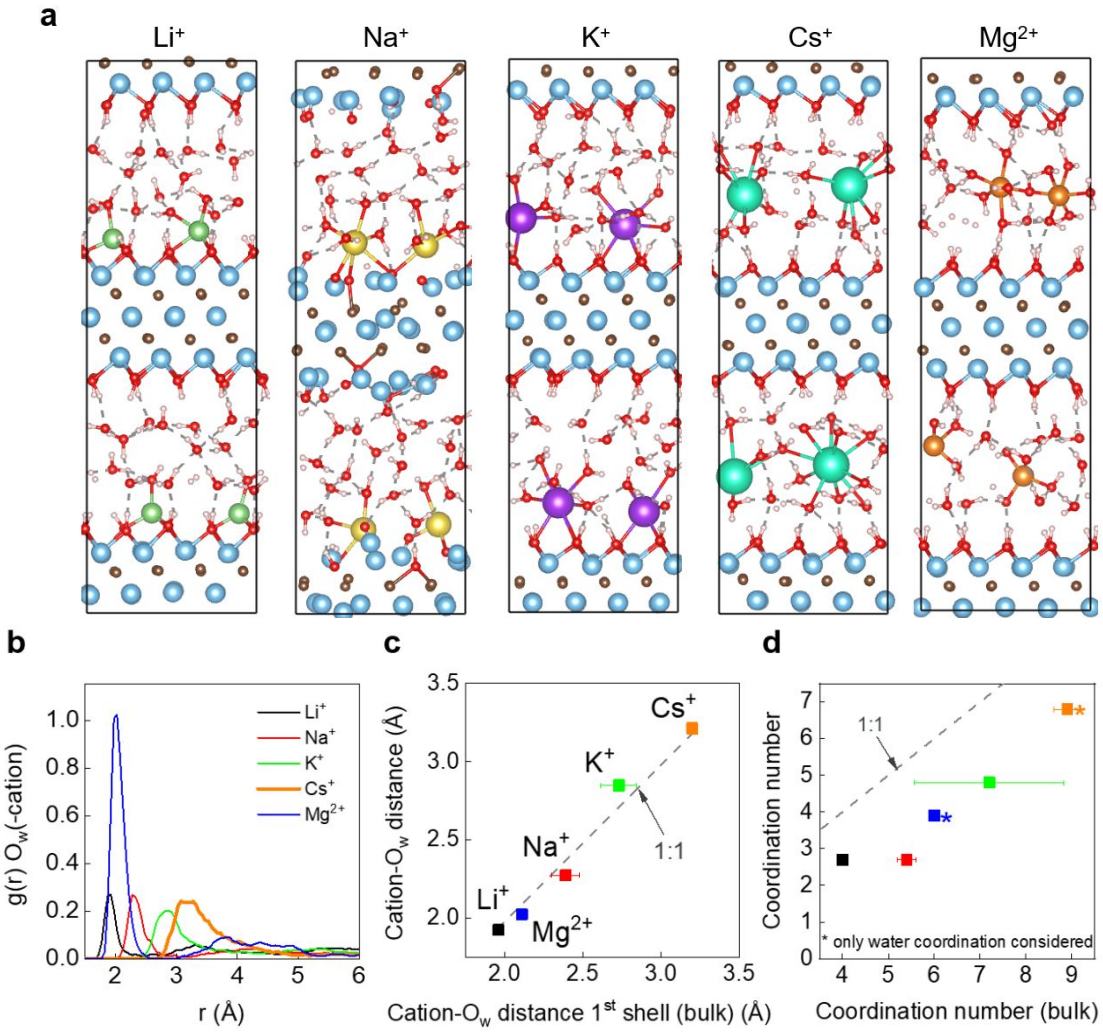

Figure 1. Cations arrangements in MXene interlayers and their interactions with water via MD simulations. (a) Cation distributions in the interlayer space. Light blue stands for Ti, dark grey for C, red for O, light pink for H. (b) Radial distribution functions of oxygen in water, *g*(*r*), Ow, around cations obtained from the

AIMD modelling. (c) The cation-Ow distances corresponding to the positions of the maxima of $g(r)$ demonstrate a clear correlation with values in bulk solutions. (d) Coordination numbers extracted from b in comparison with values for bulk solutions. The numbers for bulk solutions were taken and averaged over all values provided in ref.[34]. The grey line indicates a reference for the case when the confined CN is equal to the CN in bulk solutions, *i.e.* 1:1.

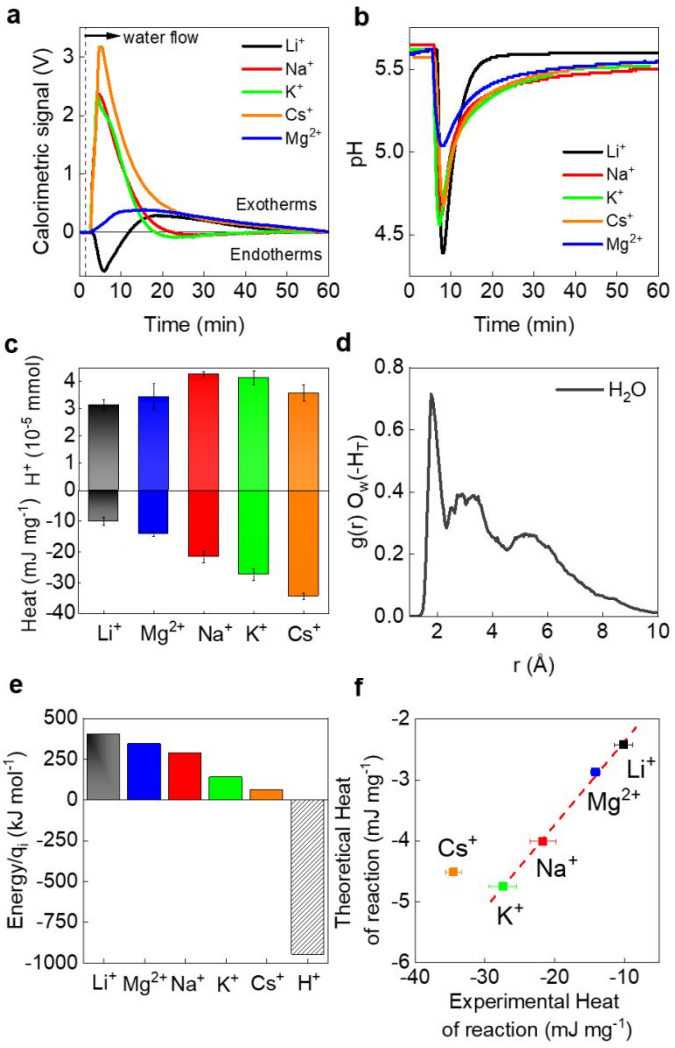

Figure 2. Energetics of cation/water exchange reactions. (a) Time dependence of the calorimetric signal during exchange between water and cations. (b) pH measurements performed during calorimetry. (c) Quantification of H^+ released as result of cations adsorbing onto the -OH sites of MXene terminations and heat of reaction determined from (a). (d) Radial distribution functions of oxygen in water, $g(r)$, Ow, around H onto termination (H_T) obtained from the AIMD simulations for pure water. (e) Energetics of cation dehydration and H^+ rehydration normalized by cation valence. q_i represents the cation valence. (f) Heat of reaction correlation between theoretically calculated using AIMD and experimentally measured using calorimetry.

The simultaneously measured changes in pH as a function of time are shown in Fig. 2b. The pH signal for Li^+ returned to the baseline faster than the other cations, which resulted in the smallest H^+ release. In Fig.2c, the HOR in mJ mg^{-1} (MXene mass) and amount of released H^+ extracted from Fig.2a-b do not show any correlation between them (Fig. 2c), but HOR itself shows a clear trend of $Li^+<Mg^{2+}<Na^+<K^+<Cs^+$. We find that the HOR have a linear relationship with the cation bulk hydration enthalpy with Mg^{2+} as outlier (Fig. S4a, ESI)[35], suggesting the studied cations interaction with MXene are undergoing processes involving their hydration shells.

For a semi-quantitative analysis, the HOR is governed by the cation dehydration and the proton hydration, which can be estimated according to the CN theory based on AIMD results. For this, we take advantage of the CN of cations by surrounding water oxygen (Fig.S3) and CN of the surface protons (H_T) extracted from *g(r)* functions (Fig. 2d) for the endothermic and exothermic parts to model the measured HOR. Here, we only consider the CN from the water oxygen and neglect the adsorption energies onto MXene. Table 1 summarized the CN in bulk solutions[34, 36], CN for ions confined in MXene interlayers, bulk hydration enthalpies[37, 38], and total energy gain/loss per mol due to cation dehydration and proton hydration. The corresponding energies normalized by cation charge are shown in Fig. 2e and are calculated based on the fractional change in CN with respect to the full hydration energy. It shows a linear correlation for HOR between calorimetry and theoretical modelled cation dehydration (Fig. S4b), implying relatively constant heat contributions from H^+ rehydration amongst the studied cations. The exothermic proton hydration is much larger than all endothermic cation dehydration processes resulting in a net negative HOR. To calculate the net energy, we use the measured concentration of released protons to determine the quantity of intercalated cation concentration under assumption of net zero charge. Comparing the measurements with theoretical modelled values, we find a qualitative linear correlation between experiment and theory with Cs^+ as an outlier (Fig. 2f) but the energy scales differ by a factor of 4.2-7.6. We believe that the majority of this difference is due to the simplified picture of AIMD model and CN theory analysis, *e.g.*, the CN-dependent hydration energies solvated hydronium complexes, in which AIMD is restricted to a limited number of sites while calorimetry experiments average over a larger numbers and potentially energetical different sites[39]. Additionally, varying intercalation barriers representing the intercalation into different depths of the multilayer electrode structure are not considered in the theoretical description. The Cs^+ outlier may result from known problems with limited electrolyte uptake[18]. The thermodynamic contributions we have discussed above provide a plausible trend of HOR indicating we have likely identified the underlying atomistic processes.

Another consequence of the cation intercalation is the change in *c*-lattice parameter[5, 6] and thus the local mechanical properties of the MXene. To study local elastic modulus and energy dissipation processes, contact resonance (CR)-AFM has been performed with 10's of nm lateral resolution. When mechanically excited, the AFM probe oscillations in contact with the surface is a function of the Young's modulus and energy dissipation as expressed by the inverse of the damping factor Q^{-1} (Fig. 3a). All results in this study were acquired with both the MXene and the AFM cantilever probe fully immersed in the aqueous electrolytes. Mapping of the contact stiffness (related to Young's modulus) has not shown clear

variations between cation types (Fig. S5, ESI). However, the experiments showed a notable effect of the cation type on the mechanical energy dissipation into MXene (Fig. 3b).

Table 1 Summary of energies variations for cation dehydration and proton hydration.

Ion	Bulk CN (A)	Confined ions' CN (B)	Bulk $E_{hydr.}$ (kJ mol^{-1}) (C)	E^* (kJ mol^{-1}) (D)
H^+	6	0.8	-1091	-945
Li^+	4	0.87	-520	407
Na^+	5.4	1.67	-409	283
K^+	7.2	3.41	-322	170
Cs^+	8.9	6.84	-264	61
Mg^{2+}	6	3.86	-1921	685

***** *Calculation Equation: D = [(A-B)/A]×C*

In the following, we will discuss mechanical energy loss through relaxations of molecular and atomic arrangements in the sample in response to elastic strains[40, 41] to focus on the energetics for the water and ions themselves rather than the reactions discussed above. The water confined between MXene layers is the main damper of the probe oscillations in MXene. It is well accepted that in the bulk solution the relaxation processes are significantly influenced by the dissolved ions as water-ion interactions affect water structure and, hence, rotational and translational mobility of the water molecules in the immediate vicinity of hydrated ions and beyond the hydration shells[34, 42]. Even though the relaxation times of water molecules are in a few picoseconds range[34, 43], the relaxation rate is reflected in the low-frequency liquid behaviour, for example, in liquid viscosity as expressed by the Stokes-Einstein-Debye equation[42], more generally relating fluid viscosity and species mobility (diffusion coefficient). In turn, the effect of ions on the water structure and viscosity is expressed through the *B* coefficient of the Jones-Dole expression relating the solution dynamic viscosity and ionic concentration[34]. Therefore, we expect a relationship between the *B* coefficient and the energy dissipation in MXene. In Fig. 3c, we plot the energy dissipation relative to DI water normalized by ion concentration with the *B* coefficient. While the exact amount of spontaneously intercalated cations is unknown, it was found that after long exposure times of MXene to electrolytes, the amounts of spontaneously intercalated Mg^{2+} and K^+ are the lowest, as quantified by X-ray photoelectron spectroscopy (XPS, Fig. S6, ESI) and energy-dispersive X-ray spectroscopy (EDX, Fig. S7, ESI). Note that the error bars in Fig. 3c indicate variations across the sample surface, uncertainty of the measurement at a single pixel is much smaller. Fig. 3c shows the linear correlations with the fitting line passes through the origin of the coordinate system. The opportunities which arise from the link of cation and mechanical energy losses include the capability to map ion distribution on 10s of nanometers length scales as shown in Fig. 3d for Li^+. It can be seen that the energy dissipation for Li^+ is heterogeneous and patches of high energy loss appear across the sample surface. Accordingly, these can be interpreted as accumulation of Li^+ inside the MXene probed in the near surface regions. Images of other cations are given in Fig. S8, ESI. This approach provides future accessibility to track the local energy storage processes under electrochemical cycling.

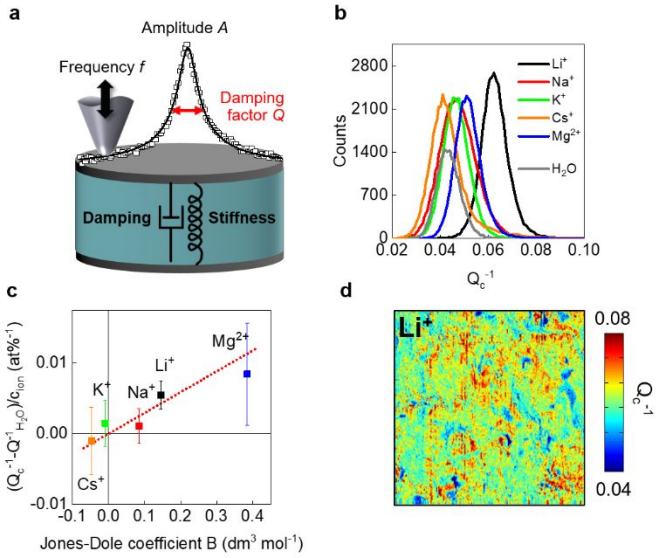

Figure 3. Energy losses driven by cations in confinement. (a) Schematic of CR-AFM. (b) Measured distribution of energy dissipation Q_c^{-1} of the sample under mechanical vibrations as a function of electrolyte. (c) Change in energy dissipation relative to pure water normalized by ionic concentration and plotted versus the Jones-Dole coefficient *B*. (d) Spatial map (size 10×10 μm) of local energy losses measured in 0.5 M Li_2SO_4 recorded at the immersed time point of two hours.

To shed light on the charge storage mechanism, we explore the link between cation-MXene distance and capacitance measured by cyclic voltammograms (CVs) at 5 mV s^{-1} in a three-electrode cell configuration (Fig. 4a). The rectangular shaped CVs suggest the main charge storage mechanism is EDL[11, 18]. Once the cations intercalate into MXene, they occupy preferable sites of MXene layers that are at different distances from the MXene surface as probed via the RDF of cation around the termination oxygen (-O_T) taken as a reference point for the MXene surface (Fig. 4b). Li^+ is the closest to the surface followed by Na^+ and K^+. This series of trend found in *g(r)* is qualitatively the same trend in previous ReaxFF-based studies[24]. We correlate the measured capacitance at the OCP averaged over the charge and discharge curves (Fig. S9, ESI) with the cation-O_T distance *d* suggested by the Helmholtz model ($C = \varepsilon\varepsilon_0/d$, where *C* is the capacitance, ε and ε_0 are the dielectric constant and the vacuum permittivity, and *d* is the distance from the ion to the EDL), as determined from the positions of the major peak in the *g(r)*. We chose the capacitance at OCP as the closest to the theoretical results which were obtained without external potential applied. Interestingly, we observe a linear relationship between capacitance at OCP and the inverse cation-O_T distance *d* with an intercept of 39.9±6.6 F g^{-1} (Fig. 4c). To rationalize the residual intercept capacitance, we propose a modified Helmholtz model that considers two double layers contributed by two MXene surfaces for each slit

pore. Fig. 4d shows the confined space of width $W=d_1+d_2$ sandwiched by two MXene surfaces of the same area A. Assuming the individual MXene sheets are electrically connected (*i.e.*, they have the same potential), an equivalent circuit containing two parallel capacitors with a distance of d_1 and d_2 is obtained. Note that d_1 is the closest distance between cation and MXene surface and extracted from *g(r)*. Since the two capacitors are connected in parallel, the total capacitance measured by CVs is simply the sum of the contributions from the two MXene surfaces. After determining the width W from AIMD (Fig. 4e), we decompose the total capacitance to C_1 and C_2 derived from d_1 and d_2 $(W-d_1)$ for best statistics from the simulations. When plotted individually over $1/d$, a linear relationship is derived with an intercept of -6.1 ± 5.4 F g^{-1}, *i.e.*, the fit goes through the graph's origin (Fig. 4f). The two parts of the total capacitance, C_1 and C_2 derived from d_1 and d_2 respectively are showing an almost identical slope, which is the product of $\varepsilon\varepsilon_0$, suggesting the nearly identical dielectric constants for ε_1 and ε_2. The most interesting observation is that the C_2 capacitance is comparable for all cations and is concentrated around 40-50 F g^{-1}, which is very close to the capacitance intercept in Fig. 4c, suggesting that the capacitance intercept originates from the capacitance of the surface associated with d_2. The resulting total capacitance C_{tot} is determined by $\varepsilon\varepsilon_0(1/d_1+1/d_2)$, presented as the modified Helmholtz model. Thus, the location of cations under confinement is needed to fully explain the observed energy storage properties.

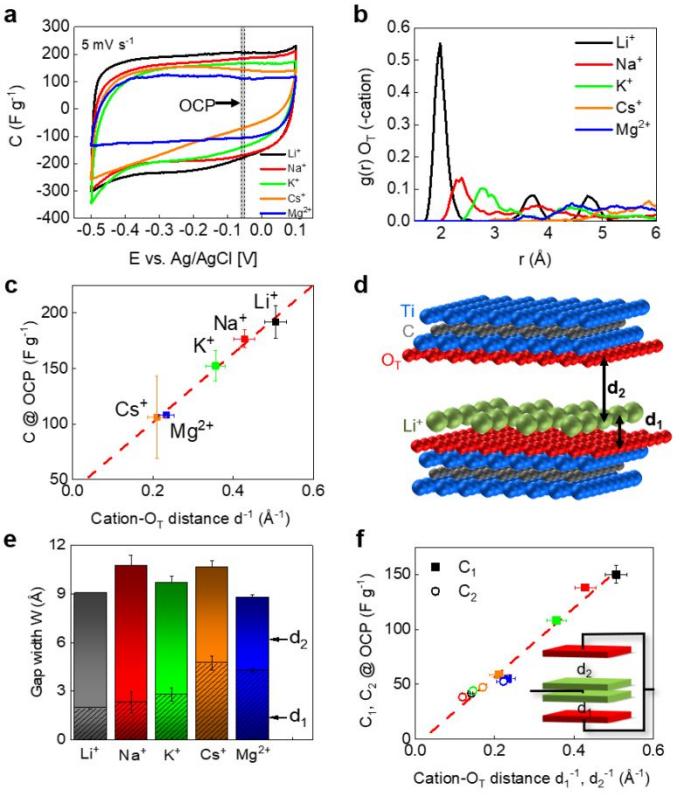

Figure 4. Cations interactions with MXene result in the variations of electrochemical performance. (a) Cyclic voltammograms (5 mV s^{-1}) for different cations in 0.5 M sulfate solutions. The thermodynamic potential for water reduction is around -0.59 V vs. Ag/AgCl, suggesting there is no redox water reduction involved. (b) The cation radial distribution functions with respect to oxygen on the MXene surface. (c) Relationship between cation-MXene distance^{-1} corresponding to d^{-1} and averaged capacitance at OCP. (d) The schematic of modified Helmholtz model in two MXene layers. d_1 and d_2 vary with aqueous cations. (e) The confined space of width $W= d_1+d_2$ determined from AIMD modelling. (f) Relationship between C_1 and C_2, and the corresponding inverse distance of $1/d_1$ and $1/d_2$, respectively, at OCP. Inset: an equivalent circuit containing two parallel capacitors with a distance of d_1 and d_2 is obtained.

Conclusions

Given the complex nature of interactions between electrolyte and electrode in confinement, the observed trends and modulated interactions between the cations and MXene surfaces hold promise for broader application in layered materials with nanoconfined fluids. Under strong confinement, the system is dominated by the cation hydration and cation exchange with surface termination groups (cation adsorption). The demonstrated cation-MXene interaction for aqueous cations has consequences for macroscopic material behaviour such as cation exchange energetics, mechanical energy losses which can be employed in the future to study spatial variations of the intercalation process and electrochemical capacitance. For the latter, we directly demonstrate that the average distance between the cation and MXene surface follows a *1/d* relationship when plotted versus the open circuit potential capacitance. We proposed the modified Helmholtz model to elucidate the EDL mechanism for MXenes which is applicable to a wide range of aqueous electrolytes and layered materials. The capture of rational coordination number of hydration of ions and protons is the key of understanding energetics under confinement. These highlight the importance of understanding the cation-water-MXene interactions under confinement in order to get a complete understanding of MXenes' energy storage properties and processes. This is only possible when experiment and *ab-initio* theory with the framework of having explicit water and solid-liquid interactions well described are combined and analysed together to reveal the relevant relationships. The demonstrated approaches and findings enhance our understanding of the energy storage in 2D materials and help to guide further development in the large MXenes family. We further anticipate that the integrated research will be rapidly adopted to enable understanding and manipulating behaviours of ions and confined fluids for electrochemical energy storage, water desalination, and ion-selective membranes.

Experimental

MXene synthesis. MXene was synthesized by etching Al from Ti_3AlC_2 using a mixture of LiF and HCl as reported previously[44]. In short, 6 g of LiF was dissolved in 90 mL of 6M HCl aqueous solution, then a total amount of 9 g of Ti_3AlC_2 (particle size < 45 micron) was added in small portions gradually to the solution at room temperature. Afterward, the reaction vessel was moved to an oil bath that was kept at 40 °C. Teflon coated magnetic stir bar was used to stir the solution during

the reaction. After 45 h, the reaction was stopped, and the suspension was centrifuged (at 3500 rpm) to separate the powders from the solution. Then, fresh DI water was added and followed by centrifugation to washout the residual acids and etching products. The step of adding fresh DI water and centrifuging was repeated till the pH of the decanted liquid after centrifuging was higher than 4. The chemical compositions turned out to be $Ti_3C_2F_{0.79}Cl_{0.15}O_{1.06}Li_{0.16}$, in which the Ti:Li was estimated from inductively coupled plasma mass spectrometry analysis and the rest from EDX analysis.

The sedimented powder paste after washing was transferred to vacuum-assisted filtration setup to dry the powders. To prepare free-standing MXene paper, 1 g of Ti_3C_2-clay was added to 20 mL of DI water and sonicated for 1 h then centrifuged at 3500 rpm and the black dispersion of MXene in DI water was decanted and filtered through a Celgard membrane. After allowed to dry at RT the free-standing MXene film was peeled off the membrane.

Computational MD simulations. We performed *ab initio* molecular dynamics in Vienna atomic simulation package (VASP)[45, 46] within the all-electron projector augmented wave (PAW) method[47] for all calculations. The van der Waals density functional of optB86b was included to describe the inter-layer dispersive forces[48]. The cut-off energy was set to 450 eV, and structural optimizations were converged to $1e^{-6}$ eV in energy and 0.03 eV/Å in force residuals. A 1 × 1 × 1 gamma-centred **k** mesh grid was used to sample the Brillouin zone. The AIMD simulations have been performed in the NPT (constant number of atoms (N), constant pressure (P) of ambient conditions and constant temperature (T) of room temperature) ensemble, with a time step of 1 fs using the Langevin thermostat[49, 50]. The AIMD eventually reaches the timescale at 18 ps, in which the first 12 ps was removed to account for equilibrations, and the last 6 ps subsequently analysed.

The structure model considers multiple-layered hydroxyl terminated MXenes in a 2 × 2 × 1 orthogonal supercell containing 244 atoms (containing four metal ions) with in-plane lattice parameters *a*, *b* of about 6 and 12 Å and the varying *c*-LP ~ 30 Å. We assume the MXenes are fully covered by a bilayer of water giving a chemical formula of $Ti_3C_2(OH)_2(H_2O)_2$. For the initial positions of metal ions, we compared four symmetry inequivalent sites, and took the lowest energy configurations. Due to the slight energetic differences between considered sites of ions, we used 4×4×1 gamma-centred **k** mesh grids for the Brillouin zone sampling in this comparison to achieve a convergence of about 3 meV. Note that the inserted cations were treated as neutral atoms, and the stacking of water molecules are consistent with earlier studies[26]. The data after 10 ps, in where we started taking statistics, has been used for analysing till signal was equilibrated after that time (Fig. S10, ESI). The number of cations was kept constant for all cations for better comparison and was guided by the analysis shown in Fig. S7.

AFM measurements. CR-AFM measurements were conducted on a Cypher AFM (Oxford Instruments, UK) in air and liquid environments using the band excitation BE approach during scanning in contact mode. A 200 kHz wide frequency excitation band was sent to the cantilever probe with a "*BlueDrive*^{TM}" photothermal laser focused at the base of the cantilever. The cantilever response was detected and then Fourier transformed to extract the contact resonance peak. The probe used in this study was a gold-coated silicon probe (PPPFM-Au, Nanosensors, USA) with a spring constant k_c ~ 3 N/m and a free resonance frequency in air f_0 ~ 65 kHz. Typical parameters for the cantilever probe employed were: L = 225 µm, L_1 = 215 µm, h = 12 µm, and cantilever tilt angle = 12°. The perfusion cantilever holder from Asylum Research USA was used throughout our measurements. The contact resonance frequency f and quality factor Q were extracted from each contact resonance curve via fitting with a simple harmonic oscillator (SHO) model. Tip calibrations were conducted in air and in an 18 MΩ deionized water on reference samples (freshly cleaved HOPG, Bruker, Germany). Aqueous 0.5 mol L^{-1} Li_2SO_4, Na_2SO_4, Cs_2SO_4, K_2SO_4, $MgSO_4$ were used as electrolytes. During the CR-AFM, the cantilever and the studied MXene paper were fully immersed into the electrolytes.

The damping of the mechanical vibrations due to energy dissipation in the sample Q_c^{-1} is calculated using the equation $Q_c^{-1} = Q^{-1} - Q_{fluid}^{-1}$, where Q is the quality factor of the measured contact resonance in solution, and Q_{fluid}^{-1} is the damping due to the liquid. Q_{fluid}^{-1} are determined for the DI water and each of the electrolyte solutions via hydrodynamic functions. The equations for the estimation and application of the hydrodynamic function, correction and calculation of loss tangent, equations from Ref. [51] were used. This is necessary to separate sample from electrolyte effects. To excite flexural cantilever resonances, the power of the photothermal excitation laser of the AFM microscope (*Blue Drive*, Cypher, Asylum Research) was modulated with amplitudes of 1 mW in air and 2 mW in solutions. For non-contact, near-surface data collection, the cantilever was positioned near the surface by first touching the surface with the tip and then retracting the cantilever by approximately 150 nm. The control for this distance is accomplished with the help of the single-point force-distance-curve programming developed in house. Because this distance is less than 2% of the height of the probe tip (about 15µm), the distances between the probe cantilever and the surface are very close for the contact measurement and the near-surface measurement. Thus, the probe hydrodynamics should be similar as well, once we account for frequency and cantilever vibrational shape effects. All the correction measurements have been performed with the Band Excitation technique up to a 2 MHz excitation frequency. The calibration procedure described above and the fact that bulk properties determine the vibrational sample response with the used contact forces[52, 53] ensure the probing of material properties instead of surface properties.

Flow microcalorimetry experiments. The interactions of cations with MXene were probed using flow microcalorimetry in tandem with *in situ* pH measurements. In addition to the heats in mJ mg^{-1} (MXene mass), of adsorption/intercalation reactions, the mass of H^+ involved was also quantified to probe underlying differences between cations.

The flow microcalorimeter (FMC) used was custom-designed and fabricated in the Kabengi laboratory (Prof. Dr. Nadine Kabengi, Georgia State University). The flow microcalorimeter consists of a micro-column which is sealed inside a 500-mL bottle and is immersed in an insulated container filled with water and maintained at room temperature. Solution containing the species of interest was allowed to flow through the packed column at flow rates between 0.30- and 0.35-mL min^{-1} until a steady baseline is obtained.

Two thermistors located on the upstream and the other downstream from the column, sensed temperature changes in the solution as it passed through the column. Any changes in solution temperature from heat evolved or consumed as a result of either physical or chemical interactions between the reacting solution and the solid produce a differential output voltage, which was amplified and fed into a computer for processing where they are displayed graphically and recorded as a function of time. The end of reaction is demonstrated by the return of the calorimetric signal to the initial baseline.

The heats of reactions (Q in mJ mg^{-1} solid) are determined by integrating the calorimetric peaks to obtain flow rate-averaged peak areas, which are converted to energy units (Joules) by comparison to peaks of known energy input generated from a calibrating resistor located within the flow stream inside the micro-column. A MXene sample of known mass (7.0 ± 0.1 mg) was homogeneously packed into the FMC's micro-column and equilibrated with 18.2 MΩ deionized water adjusted at a pH of 5.6 ± 0.2 to obtain thermal equilibrium. Then, the input solution (water) was changed to a solution containing the cation of interest at 0.5 mol L^{-1}, *i.e.* either Li_2SO_4, Na_2SO_4, K_2SO_4, Cs_2SO_4, or $MgSO_4$, adjusted to the same pH using the corresponding hydroxide solution (*i.e.,* 0.1 M of LiOH, NaOH, KOH, CsOH and, Mg $(OH)_2$) and the Q_{rxn} for each cation were obtained. Multiple replicates for each cation were made to establish the reproducibility of the measurements. During all experiments, the effluent pH was monitored using a flat surface pH probe (S450CD, Sensorex; OrionStar A215 pH meter, Fisher Scientific) connected in line to the effluent line of the FMC and which continuously recorded pH as a function of time. The mmol of H^+ was calculated by converting the pH measurements to the hydrogen ion concentrations and integrating over the time measured. The integrated values were then multiplied by corresponding flow rates. For calculating the number of H^+, the same integration was applied for a constant pH of 5.60. The difference between the two values was determined and taken as the H^+ differential, ΔH^+.

Electrochemical characterizations. An ECD-3-Nano (EL CELL®, Germany) three electrode cell was employed to perform cyclic voltammetry (5 mV s^{-1}) of free-standing MXene film electrodes (2 um) in aqueous 0.5 mol L^{-1} Li_2SO_4, Na_2SO_4, Cs_2SO_4, K_2SO_4, $MgSO_4$ electrolytes. The electrolytes compared in this study were prepared to have the same cation charge instead of cation number concentration since the charge is the relevant property for electrode charge compensation. The cell was connected to a potentiostat (VSP 200, Bio-Logic S.A., France). An activated carbon film (YP50F, Kuraray, Japan) was used as a counter electrode as well as the quasi-reference electrode reference electrode (0.1 V *vs.* Ag/AgCl). The capacitance of MXene electrode was calculated from the CV curve from the following equation:[12]

$$C\ (F\ g^{-1}) = \frac{\int i * dt}{mV}$$

Conflicts of interest

The authors declare no competing financial interests.

Acknowledgements

This work was supported as part of the Fluid Interface Reactions, Structures and Transport (FIRST) Center, an Energy Frontier Research Center funded by the U.S. Department of Energy, Office of Science, Office of Basic Energy Sciences. CR-AFM of this research was conducted at the Center for Nanophase Materials Sciences, which is a DOE Office of Science User Facility. This research used resources of the National Energy Research Scientific Computing Center (NERSC), a U.S. Department of Energy Office of Science User Facility operated under Contract No. DE-AC02-05CH11231. CR-AFM data analysis was partially supported within the scope of the project CICECO-Aveiro Institute of Materials, FCT Ref. UID/CTM/50011/2019, financed by national funds through the FCT/MCTES. Discussions with Netanel Shpigel are highly appreciated.

Author contributions

M.N., M.A. and Y.G. prepared the MXene sample and provided fruitful discussions on the properties of MXene. P.I., N.K., N.B. and Q.G. designed the experiments and P.I. and Q.G. conducted the experiments. W.S., J.H. and P.K. performed AIMD simulations and proposed theoretical models. A.T. and S.J. developed the microscopic measurements and analysis tools. A.B. tested XPS and performed the data analysis. Q.G. and N.B. wrote the initial manuscript. All authors discussed the results and commented on the manuscript. Q.G. and W.S. contribute equally.

Notes and references

1. V. Augustyn and Y. Gogotsi, *Joule*, 2017, **1**, 443-452.
2. V. Augustyn, J. Come, M. A. Lowe, J. W. Kim, P. L. Taberna, S. H. Tolbert, H. D. Abruna, P. Simon and B. Dunn, *Nat Mater*, 2013, **12**, 518-522.
3. E. Pomerantseva and Y. Gogotsi, *Nature Energy*, 2017, **2**, 17089.
4. M. Naguib, V. N. Mochalin, M. W. Barsoum and Y. Gogotsi, *Advanced Materials*, 2014, **26**, 992-1005.
5. B. Anasori, M. R. Lukatskaya and Y. Gogotsi, *Nature Reviews Materials*, 2017, **2**, 16098.
6. M. R. Lukatskaya, O. Mashtalir, C. E. Ren, Y. Dall'Agnese, P. Rozier, P. L. Taberna, M. Naguib, P. Simon, M. W. Barsoum and Y. Gogotsi, *Science*, 2013, **341**, 1502-1505.

7. M. Ghidiu, M. R. Lukatskaya, M. Q. Zhao, Y. Gogotsi and M. W. Barsoum, *Nature*, 2014, **516**, 78-81.
8. M. R. Lukatskaya, S. Kota, Z. Lin, M.-Q. Zhao, N. Shpigel, M. D. Levi, J. Halim, P.-L. Taberna, M. W. Barsoum, P. Simon and Y. Gogotsi, *Nature Energy*, 2017, **2**, 17105.
9. Y. Xia, T. S. Mathis, M.-Q. Zhao, B. Anasori, A. Dang, Z. Zhou, H. Cho, Y. Gogotsi and S. Yang, *Nature*, 2018, **557**, 409-412.
10. M. R. Lukatskaya, S.-M. Bak, X. Yu, X.-Q. Yang, M. W. Barsoum and Y. Gogotsi, *Advanced Energy Materials*, 2015, **5**, 1500589.
11. M. Hu, Z. Li, T. Hu, S. Zhu, C. Zhang and X. Wang, *ACS Nano*, 2016, **10**, 11344-11350.
12. X. Wang, T. S. Mathis, K. Li, Z. Lin, L. Vlcek, T. Torita, N. C. Osti, C. Hatter, P. Urbankowski, A. Sarycheva, M. Tyagi, E. Mamontov, P. Simon and Y. Gogotsi, *Nature Energy*, 2019, **4**, 241-248.
13. Q. Gao, L. Demarconnay, E. Raymundo-Pinero and F. Beguin, *Energy & Environmental Science*, 2012, **5**, 9611-9617.
14. M. He, K. Fic, E. Fŗckowiak, P. Novák and E. J. Berg, *Energy & Environmental Science*, 2016, **9**, 623-633.
15. M. Ghidiu, S. Kota, J. Halim, A. W. Sherwood, N. Nedfors, J. Rosen, V. N. Mochalin and M. W. Barsoum, *Chemistry of Materials*, 2017, **29**, 1099-1106.
16. N. C. Osti, M. Naguib, A. Ostadhossein, Y. Xie, P. R. C. Kent, B. Dyatkin, G. Rother, W. T. Heller, A. C. T. van Duin, Y. Gogotsi and E. Mamontov, *Acs Applied Materials & Interfaces*, 2016, **8**, 8859-8863.
17. E. S. Muckley, M. Naguib, H.-W. Wang, L. Vlcek, N. C. Osti, R. L. Sacci, X. Sang, R. R. Unocic, Y. Xie, M. Tyagi, E. Mamontov, K. L. Page, P. R. C. Kent, J. Nanda and I. N. Ivanov, *ACS Nano*, 2017, **11**, 11118-11126.
18. N. Shpigel, M. D. Levi, S. Sigalov, T. S. Mathis, Y. Gogotsi and D. Aurbach, *Journal of the American Chemical Society*, 2018, **140**, 8910-8917.
19. A. Sugahara, Y. Ando, S. Kajiyama, K. Yazawa, K. Gotoh, M. Otani, M. Okubo and A. Yamada, *Nature Communications*, 2019, **10**, 850.
20. M. Ghidiu, J. Halim, S. Kota, D. Bish, Y. Gogotsi and M. W. Barsoum, *Chemistry of Materials*, 2016, **28**, 3507-3514.
21. F. Malchik, N. Shpigel, M. D. Levi, T. S. Mathis, A. Mor, Y. Gogotsi and D. Aurbach, *Journal of Materials Chemistry A*, 2019, **7**, 19761-19773.
22. N. Shpigel, M. R. Lukatskaya, S. Sigalov, C. E. Ren, P. Nayak, M. D. Levi, L. Daikhin, D. Aurbach and Y. Gogotsi, *Acs Energy Letters*, 2017, **2**, 1407-1415.
23. M. D. Levi, M. R. Lukatskaya, S. Sigalov, M. Beidaghi, N. Shpigel, L. Daikhin, D. Aurbach, M. W. Barsoum and Y. Gogotsi, *Advanced Energy Materials*, 2015, **5**, 1400815.
24. N. C. Osti, M. Naguib, K. Ganeshan, Y. K. Shin, A. Ostadhossein, A. C. T. van Duin, Y. Cheng, L. L. Daemen, Y. Gogotsi, E. Mamontov and A. I. Kolesnikov, *Physical Review Materials*, 2017, **1**, 065406.
25. J. Come, J. M. Black, M. R. Lukatskaya, M. Naguib, M. Beidaghi, A. J. Rondinone, S. V. Kalinin, D. J. Wesolowski, Y. Gogotsi and N. Balke, *Nano Energy*, 2015, **17**, 27-35.
26. J. Come, Y. Xie, M. Naguib, S. Jesse, S. V. Kalinin, Y. Gogotsi, P. R. C. Kent and N. Balke, *Advanced Energy Materials*, 2016, **6**, 1502290.
27. Q. Gao, J. Come, M. Naguib, S. Jesse, Y. Gogotsi and N. Balke, *Faraday Discussions*, 2017, **199**, 393-403.
28. A. Al-Temimy, K. Prenger, R. Golnak, M. Lounasvuori, M. Naguib and T. Petit, *ACS Appl Mater Interfaces*, 2020, DOI: 10.1021/acsami.9b22122.
29. Y. Xie, M. Naguib, V. N. Mochalin, M. W. Barsoum, Y. Gogotsi, X. Yu, K. W. Nam, X. Q. Yang, A. I. Kolesnikov and P. R. Kent, *J Am Chem Soc*, 2014, **136**, 6385-6394.
30. C. Eames and M. S. Islam, *Journal of the American Chemical Society*, 2014, **136**, 16270-16276.
31. Y. Xie and P. R. C. Kent, *Physical Review B*, 2013, **87**, 235441.
32. Y. Xie, Y. Dall'Agnese, M. Naguib, Y. Gogotsi, M. W. Barsoum, H. L. Zhuang and P. R. C. Kent, *ACS Nano*, 2014, **8**, 9606-9615.
33. C. E. Ren, K. B. Hatzell, M. Alhabeb, Z. Ling, K. A. Mahmoud and Y. Gogotsi, *The Journal of Physical Chemistry Letters*, 2015, **6**, 4026-4031.
34. Y. Marcus, *Chem. Rev.*, 2009, **109**, 1346-1370.
35. J. Mähler and I. Persson, *Inorganic Chemistry*, 2012, **51**, 425-438.
36. A. A. Zavitsas, *The Journal of Physical Chemistry B*, 2001, **105**, 7805-7817.
37. D. W. Smith, *Journal of Chemical Education*, 1977, **54**, 540.
38. N. Allen, M. L. Machesky, D. J. Wesolowski and N. Kabengi, *Journal of Colloid and Interface Science*, 2017, **504**, 538-548.
39. N. J. Kabengi, M. Chrysochoou, N. Bompoti and J. D. Kubicki, *Chemical Geology*, 2017, **464**, 23-33.
40. A. S. Nowick, *Anelastic Relaxation In Crystalline Solids*, Elsevier Science, 2012.
41. Y. Hiki and J. Tamura, *The Journal of Physical Chemistry*, 1983, **87**, 4054-4059.
42. D. A. Turton, J. Hunger, G. Hefter, R. Buchner and K. Wynne, *The Journal of Chemical Physics*, 2008, **128**, 161102.
43. R. P. W. J. Struis, J. De Bleijser and J. C. Leyte, *The Journal of Physical Chemistry*, 1989, **93**, 7943-7952.
44. M. Alhabeb, K. Maleski, B. Anasori, P. Lelyukh, L. Clark, S. Sin and Y. Gogotsi, *Chemistry of Materials*, 2017, **29**, 7633-7644.
45. G. Kresse and J. Hafner, *Physical Review B*, 1993, **48**, 13115-13118.
46. G. Kresse and J. Hafner, *Physical Review B*, 1994, **49**, 14251-14269.
47. P. E. Blöchl, *Physical Review B*, 1994, **50**, 17953-17979.
48. J. Klimeš, D. R. Bowler and A. Michaelides, *Physical Review B*, 2011, **83**, 195131.
49. W. G. Hoover, A. J. C. Ladd and B. Moran, *Physical Review Letters*, 1982, **48**, 1818-1820.
50. D. J. Evans, *The Journal of Chemical Physics*, 1983, **78**, 3297-3302.
51. A. B. Churnside, R. C. Tung and J. P. Killgore, *Langmuir*, 2015, **31**, 11143-11149.
52. P. A. Yuya, D. C. Hurley and J. A. Turner, *Journal of Applied Physics*, 2011, **109**, 113528.
53. P. A. Yuya, D. C. Hurley and J. A. Turner, *Journal of Applied Physics*, 2008, **104**, 074916.

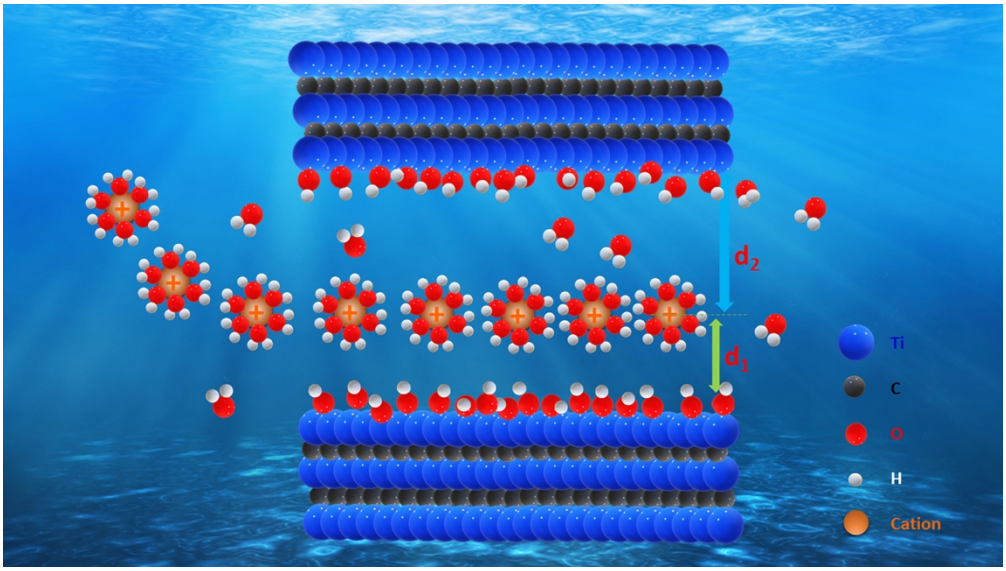

79x45mm (600 x 600 DPI)